



Extension of the finite volume particle method to viscous flow

Ruairi M. Nestor*, Mihai Basa, Martin Lastiwka, Nathan J. Quinlan

Department of Mechanical and Biomedical Engineering, National University of Ireland, Galway, Ireland

ARTICLE INFO

Article history:

Received 3 November 2007

Received in revised form 15 August 2008

Accepted 5 November 2008

Available online 19 November 2008

Keywords:

Mesh-free methods

Navier–Stokes equations

Finite volume methods

Viscous flow

Incompressible flow

ABSTRACT

The finite volume particle method (FVPM) is a mesh-free method for fluid dynamics which allows simple and accurate implementation of boundary conditions and retains the conservation and consistency properties of classical finite volume methods. In this article, the FVPM is extended to viscous flows using a consistency-corrected smoothed particle hydrodynamics (SPH) approximation to evaluate velocity gradients. The accuracy of the viscous FVPM is improved by a higher-order discretisation of the inviscid flux combined with a second-order temporal discretisation. The higher-order inviscid FVPM is validated for a 1-D shock tube problem, in which it demonstrates an enhanced shock capturing ability. For two-dimensional simulations, a small arbitrary Lagrange–Euler correction to fully Lagrangian particle motion is beneficial in maintaining a favourable particle distribution over long simulation times. The viscous FVPM is validated for two-dimensional Poiseuille, Taylor–Green and lid-driven cavity flows, and good agreement is achieved with analytic or reference numerical solutions. These results establish the viability of FVPM as a tool for mesh-free simulation of viscous flows in engineering.

© 2008 Elsevier Inc. All rights reserved.

1. Introduction

Mesh-free methods have become increasingly widespread in computational modelling of fluid mechanics. These methods represent the fluid as a set of disconnected particles or points rather than as a mesh of nodes with pre-defined connectivity, and usually allow the particles to have Lagrangian motion. Mesh-free methods are particularly attractive for problems that would otherwise be complicated by the use of a mesh, such as moving boundary or free surface problems.

Smoothed particle hydrodynamics (SPH), introduced independently by Gingold and Monaghan [1] and Lucy [2], is probably the most widely used mesh-free method for fluid dynamics. SPH is a fully Lagrangian technique which was originally developed for problems in astrophysics, but recently has seen application in engineering computations, particularly for free surface problems, e.g. [3]. Numerous extensions to the basic SPH method have been proposed in the literature. Cummins and Rudman [4] introduced an incompressible extension of SPH based on a pressure projection method. Viscous flows have been computed with SPH by Takeda et al. [5] and Morris et al. [6], and more recently by Sigalotti et al. [7]. A recent review of SPH is given by Monaghan [8].

In standard SPH, particle interactions are implemented in a symmetric formulation which ensures conservation. However, the SPH interpolation and gradient operations do not yield exact results even for zero-order polynomials. Liu et al. [9], Randles and Libersky [10], Bonet and Lok [11], and others have proposed alternative versions which ensure at least first-order consistency, but consequently sacrifice the conservation property. Another family of particle methods ensures conservation through a formulation based on interparticle fluxes. These include hybrid Riemann–SPH methods proposed

* Corresponding author.

E-mail addresses: malachy.nestor@nuigalway.ie (R.M. Nestor), mihai.basa@nuigalway.ie (M. Basa), martin.lastiwka@nuigalway.ie (M. Lastiwka), nathan.quinlan@nuigalway.ie (N.J. Quinlan).

by Monaghan [12] and Vila and Degond [13], the moving least-squares particle hydrodynamics method (type III) of Dilts [14,15], the smooth volume integral conservation method of Ismagilov [16], and the finite volume particle method (FVPM) introduced by Hietel et al. [17]. These methods have a similar basis, but differ in the details of their algorithms. In this article we focus on the FVPM.

In FVPM, the fluid is represented by a set of particles, which in turn are associated with normalised, overlapping, compactly supported kernel functions. The particles are viewed as discrete volumes to which the integral form of the governing equations apply. Particle interactions are defined in terms of a flux, which is weighted depending on the overlap of the kernel supports. The FVPM equations are very similar to those of conventional finite volume methods (FVMs), and the method inherits many of the desirable properties of the FVM. In contrast to the standard SPH method, the FVPM is conservative regardless of the variation in the particle smoothing lengths. The finite volume-based formulation of the method facilitates a natural introduction of boundary conditions, without the need for fictitious particles, by imposing the appropriate constraints on the boundary fluxes. In addition, the use of upwind numerical flux functions eliminates the need for empirically determined artificial viscosity coefficients in shock-capturing simulations. Both the implementation of boundary conditions and the need for artificial viscosity coefficients are problematic and undesirable characteristics of the standard SPH method.

Recent development of the FVPM has been performed by various authors. Schick [18] introduced adaptivity to the method via anisotropic kernel functions and variable kernel supports. Lamichhane [19] computed solutions to a 1-D moving boundary problem. Keck [20] and Keck and Hietel [21] extended the FVPM to incompressible flows using a projection technique, and computed solutions to an inviscid vortex advection problem. Teleaga [22] modelled an oscillating cylinder in inviscid crossflow using an arbitrary Lagrangian–Eulerian approach.

To date, the FVPM has been limited to inviscid flow and first-order accuracy. However, viscous effects are important in many flows of practical interest, and first-order accuracy is often insufficient for practical computations. In this article, we present a higher-order spatial and temporal discretisation of the method for inviscid flow, and the method is subsequently extended to the solution of viscous flows. The higher-order discretisation is validated for an inviscid compressible flow test case containing discontinuities. The viscous implementation of the method is validated for three well-known incompressible flow test cases.

2. Governing equations

The Navier–Stokes equations in conservation form can be written as

$$\frac{\partial \mathbf{U}}{\partial t} + \nabla \cdot (\mathbf{F} - \mathbf{G}) = 0, \quad (1)$$

where $\mathbf{U} = (\rho \quad \rho \mathbf{u} \quad \rho E)^T$ is the vector of conserved variables, ρ represents the fluid density, $\mathbf{u} = (u \quad v \quad w)$ is the fluid velocity vector, and $E = e + |\mathbf{u}|^2/2$ is the total energy of the fluid, comprising internal and kinetic energies. \mathbf{F} represents the inviscid flux vector

$$\mathbf{F} = \begin{pmatrix} \rho \mathbf{u} \\ \rho \mathbf{u} \otimes \mathbf{u} + p \mathbf{I} \\ \rho \mathbf{u} \left(E + \frac{p}{\rho} \right) \end{pmatrix}, \quad (2)$$

where p is the fluid pressure and \mathbf{I} is the identity tensor. The viscous flux vector \mathbf{G} is

$$\mathbf{G} = \begin{pmatrix} 0 \\ \boldsymbol{\tau} \\ 0 \end{pmatrix}. \quad (3)$$

As they are not required for the test cases presented in this article, the viscous contributions to the energy equation are omitted for brevity. $\boldsymbol{\tau}$ is the viscous stress tensor, given in two dimensions by

$$\boldsymbol{\tau} = \begin{pmatrix} 2\mu \frac{\partial u}{\partial x} - \frac{2}{3}\mu(\nabla \cdot \mathbf{u}) & \mu \left(\frac{\partial u}{\partial y} + \frac{\partial v}{\partial x} \right) \\ \mu \left(\frac{\partial u}{\partial y} + \frac{\partial v}{\partial x} \right) & \mu \frac{\partial u}{\partial x} - \frac{2}{3}\mu(\nabla \cdot \mathbf{u}) \end{pmatrix}, \quad (4)$$

where μ is the dynamic viscosity. This system of equations is supplemented by an equation of state of the form $p = p(\rho, e)$. For the compressible flow results presented in this paper, the equation of state for a calorically perfect gas is used:

$$p = (\gamma - 1)\rho e, \quad (5)$$

where γ is the ratio of specific heats. The corresponding sound speed is

$$a = \sqrt{\gamma(\gamma - 1)e}. \quad (6)$$

Incompressible fluids are modelled using the weakly compressible approach, which was introduced to SPH by Monaghan [3]. The method involves a stiff equation of state which causes pressure to react strongly to density variations in the flow. The equation of state, due to Kirkwood and Bethe [23], is

$$p = \frac{\rho_0 a_0^2}{\gamma} \left[\left(\frac{\rho}{\rho_0} \right)^\gamma - 1 \right], \tag{7}$$

where ρ_0 is a reference density, a_0 is a reference speed of sound, and $\gamma = 7$ is the usual choice for liquids. A high value of a_0 can be chosen to ensure an acceptably low Mach number, but also results in shorter timesteps and greater computational cost, due to the Courant stability criterion. When Eq. (7) is used, the energy equation is decoupled from the momentum and continuity equations.

3. The finite volume particle method

The FVPM was originally derived by Hietel et al. [17]. The derivation of the method for inviscid flow is presented briefly here, closely following Teleaga [22]. In FVPM, the fluid is represented by a set of N particles. These particles are defined by compactly supported, overlapping test functions ψ of the form

$$\psi_i(\mathbf{x}, t) = \frac{W_i}{\sum_{j=1}^N W_j}, \tag{8}$$

where $W_i = W(\mathbf{x} - \mathbf{x}_i(t), h)$ is a compactly supported kernel function for particle i , centred at \mathbf{x}_i . The compact support radius is $2h$ in keeping with the SPH convention. In regions of high particle density, the denominator in Eq. (8) is high, resulting in lower values of the test function. Thus the denominator normalises the kernel function to ensure that the test functions form a partition of unity, i.e.

$$\sum_{i=1}^N \psi_i(\mathbf{x}, t) = 1. \tag{9}$$

Each particle is associated with a volume

$$V_i = \int_{\Omega} \psi_i d\mathbf{x} \tag{10}$$

and a discrete value of any field variable ϕ

$$\phi_i = \frac{1}{V_i} \int_{\Omega} \phi \psi_i d\mathbf{x}, \tag{11}$$

which is the integral average of ϕ weighted by the test function. ϕ_i is associated with the particle barycentre \mathbf{b}_i , defined as

$$\mathbf{b}_i = \frac{1}{V_i} \int_{\Omega} \mathbf{x} \psi_i d\mathbf{x}. \tag{12}$$

To derive the FVPM, Eq. (1), without the viscous flux \mathbf{G} , is multiplied by the test function ψ_i and integrated over the fluid domain Ω :

$$\int_{\Omega} \left(\frac{\partial \mathbf{U}}{\partial t} + \nabla \cdot F(\mathbf{U}) \right) \psi_i d\mathbf{x} = 0. \tag{13}$$

Integration by parts yields

$$\frac{d}{dt} \int_{\Omega} \mathbf{U} \psi_i d\mathbf{x} = \int_{\Omega} \left(\mathbf{F}(\mathbf{U}) \cdot \nabla \psi_i + \mathbf{U} \frac{\partial \psi_i}{\partial t} \right) d\mathbf{x} - \int_{\partial\Omega} \mathbf{F}(\mathbf{U}) \psi_i d\sigma, \tag{14}$$

where σ is the boundary coordinate. The last integral on the RHS is non-zero only if the support of the test function intersects the domain boundary $\partial\Omega$. Expanding $\partial\psi_i/\partial t$ and $\nabla\psi_i$ in terms of W , we obtain

$$\frac{\partial \psi_i}{\partial t} = - \sum_{j=1}^N (\dot{\mathbf{x}}_i \cdot \mathbf{\Gamma}_{ji} - \dot{\mathbf{x}}_j \cdot \mathbf{\Gamma}_{ij}), \tag{15}$$

$$\nabla \psi_i = \sum_{j=1}^N (\mathbf{\Gamma}_{ji} - \mathbf{\Gamma}_{ij}), \tag{16}$$

where $\dot{\mathbf{x}}$ is the particle velocity and

$$\mathbf{\Gamma}_{ij} = \psi_i \frac{\nabla W_j}{\sum_{k=1}^N W_k}. \tag{17}$$

In FVPM, the particle velocity is arbitrary. Obvious choices are $\dot{\mathbf{x}} = \mathbf{0}$ for a fully Eulerian method, and $\dot{\mathbf{x}} = \mathbf{u}$ for a fully Lagrangian method. Using the expanded terms, we can re-write Eq. (14) as

$$\frac{d}{dt}(V_i \mathbf{U}_i) = \sum_{j=1}^N \int_{\Omega} \{[\mathbf{F}(\mathbf{U}) - \mathbf{U} \cdot \dot{\mathbf{x}}_i] \Gamma_{ji} - [\mathbf{F}(\mathbf{U}) - \mathbf{U} \cdot \dot{\mathbf{x}}_j] \Gamma_{ij}\} d\mathbf{x} - \int_{\partial\Omega} \mathbf{F}(\mathbf{U}) \psi_i d\sigma. \quad (18)$$

If \mathbf{U} varies only slightly around the average $\bar{\mathbf{U}}$ on the intersection of i and j we can write Eq. (18) as

$$\frac{d}{dt}(V_i \mathbf{U}_i) \approx - \sum_{j=1}^N [\mathbf{F}(\bar{\mathbf{U}}) - \bar{\mathbf{U}} \cdot \bar{\dot{\mathbf{x}}}] \int_{\Omega} (\Gamma_{ij} - \Gamma_{ji}) d\mathbf{x} - \int_{\partial\Omega} \mathbf{F}(\mathbf{U}) \psi_i d\sigma = - \sum_{j=1}^N \beta_{ij} [\mathbf{F}(\bar{\mathbf{U}}) - \bar{\mathbf{U}} \cdot \bar{\dot{\mathbf{x}}}] - \int_{\partial\Omega} \mathbf{F}(\mathbf{U}) \psi_i d\sigma, \quad (19)$$

where $\bar{\dot{\mathbf{x}}}$ is the average particle velocity of particles i and j , and the geometric coefficient β_{ij} is defined as

$$\beta_{ij} = \gamma_{ij} - \gamma_{ji} \quad (20)$$

and

$$\gamma_{ij} = \int_{\Omega} \Gamma_{ij} d\mathbf{x}. \quad (21)$$

β_{ij} are geometric coefficients which weight the interaction of a pair of particles, and are evaluated using numerical integration in the overlap region between each pair of particles. Their value depends on the test function overlap and the surrounding particle distribution. Introducing $\mathcal{F}(\mathbf{U}_i, \mathbf{U}_j)$ to denote a numerical approximation to the inviscid flux $\mathbf{F}(\bar{\mathbf{U}}) - \bar{\mathbf{U}} \cdot \bar{\dot{\mathbf{x}}}$, the semi-discrete form of the FVPM can be written as

$$\frac{d}{dt}(V_i \mathbf{U}_i) = - \sum_{j=1}^N \beta_{ij} [\mathcal{F}(\mathbf{U}_i, \mathbf{U}_j)] - \rho_i^b \mathcal{F}_i^b, \quad (22)$$

where β_i^b is the geometric coefficient for the particle-boundary interaction and \mathcal{F}_i^b is an approximation for the boundary flux. Following Keck [20] and Keck and Hietel [21], the boundary coefficient for particle i is

$$\beta_i^b = - \sum_{j=1}^N \beta_{ij}. \quad (23)$$

Conditions are imposed on the inviscid flux to satisfy the appropriate boundary conditions. For a solid wall boundary, the convective flux is zero, which leaves only the pressure term in the inviscid flux. Following Telega [22], the inviscid boundary flux for a particle i is based on a zero-order extrapolation of the particle pressure to the wall:

$$\mathcal{F}_i^b = \begin{pmatrix} 0 \\ p_i \mathbf{n}_{ib} \\ 0 \end{pmatrix}, \quad (24)$$

where \mathbf{n}_{ib} is the unit normal vector at the boundary pointing out of the domain.

The appearance of the particle volume in Eq. (22) means that an additional equation is required for the rate of change of the particle volume. This can be obtained by differentiating Eq. (10) with respect to time, yielding

$$\frac{d}{dt} V_i = \sum_{j=1}^N [\gamma_{ij} \cdot \dot{\mathbf{x}}_j - \gamma_{ji} \cdot \dot{\mathbf{x}}_i]. \quad (25)$$

First-order temporal accuracy is achieved if the transient term in Eq. (22) is discretised using, for example, an explicit Euler approach. First-order spatial accuracy is obtained if the numerical flux function \mathcal{F} is computed on the basis of a zero order extrapolation of the discrete particle values to the particle interfaces. This combination has been used in previous FVPM work, and throughout this paper we refer to it simply as the first-order version of the method.

Hietel et al. [17] and Telega [22] have shown that the FVPM enforces global conservation, i.e.

$$\frac{d}{dt} \left(\sum_{i=1}^N V_i \mathbf{U}_i \right) = - \int_{\partial\Omega} \mathbf{F} d\sigma, \quad (26)$$

provided that the numerical flux function \mathcal{F} and the geometric coefficients satisfy certain conditions. The numerical flux function must satisfy the symmetry condition

$$\mathcal{F}(\mathbf{U}_i, \mathbf{U}_j) = -\mathcal{F}(\mathbf{U}_j, \mathbf{U}_i), \quad (27)$$

which is typically the case for numerical flux functions developed for finite volume methods. The geometric coefficients must satisfy the following two conditions:

$$\beta_{ij} = -\beta_{ji}, \tag{28}$$

$$\sum_{i=1}^N \beta_{ij} = 0. \tag{29}$$

Condition (28) ensures that particle interactions are symmetric, and condition (29) is analogous to the requirement in the conventional FVM that the faces of a finite volume form a closed surface. Condition (29) is difficult to satisfy in practice because errors are introduced by numerical integration of Eq. (20). Violation of the conditions has been shown to result in unphysical oscillations in shock tube results [20,22,24]. While it is possible to use highly accurate numerical integration to compute the coefficients, this would be prohibitively expensive in terms of computational effort. Correction procedures have been proposed by Keck and Hietel [21] and Teleaga [22], which allow conditions (28) and (29) to be satisfied without resort to highly accurate numerical integration. The correction of Teleaga [22] is used for the results presented in this paper, and the geometric coefficients β_{ij} are computed using a Gaussian quadrature procedure. 6^D integration points are used in each particle overlap region, where D is the number of space dimensions. Numerical experiments on the problems considered in this paper have shown us that less than 6^D points yields inaccurate results, even if a correction procedure is employed. Additional properties of the FVPM are discussed in [17,20,22] and also by Junk and Struckmeier [25], who proved that the method is Lax–Wendroff consistent.

Several choices are available for the kernel function. Teleaga [22] has used both piecewise linear and quadratic kernel functions, and Schick [18] has investigated the use of anisotropic kernels with non-circular supports. The kernel employed in this paper is a parabolic function, defined for SPH purposes by Fulk and Quinn [26]:

$$W(\mathbf{x} - \mathbf{x}_i(t), h) = \begin{cases} 4 - \left|\frac{\mathbf{x} - \mathbf{x}_i}{h}\right|^2, & \text{if } \left|\frac{\mathbf{x} - \mathbf{x}_i}{h}\right| < 2, \\ 0, & \text{otherwise.} \end{cases} \tag{30}$$

This choice of kernel function was motivated by numerical experiments in 1-D, which showed that this kernel was less sensitive to the number of integration points used for numerical computation of the geometric coefficients by Eq. (21).

4. Viscous extension of the FVPM

In the literature to date, the FVPM has been limited to inviscid flows. However, in many flows of practical interest, viscous effects play an important role. In this section, the extension of the FVPM to viscous flows is presented. In the viscous test cases presented later in this paper, we have found that the accuracy of the first-order FVPM becomes marginal at higher Reynolds numbers, where the flows are increasingly convection-dominated. A higher-order discretisation of the inviscid fluxes has been developed, in combination with a two stage predictor–corrector scheme for the transient terms, and has been found to improve the accuracy of the method at higher Reynolds numbers. The details of the higher-order inviscid flux and temporal discretisations are presented in this section also.

4.1. Higher-order inviscid flux discretisation

The FVPM for inviscid compressible flow, in previous versions, has been limited to first-order accuracy in space. The flux between a pair of particles has been computed using a zero-order reconstruction of particle values to the particle–particle interface. In conventional FVMs, higher orders of accuracy are obtained by using linear reconstruction of particle values to the element interfaces for the purposes of computing the inviscid fluxes, an approach introduced by van Leer [27]. In the current work, the FVPM is extended to a higher order of accuracy using this approach. This requires that the gradients of velocity, density and pressure (and temperature, where required) are computed within each particle. Similar techniques are used in dissipative particle dynamics (DPD) for mesoscopic simulations, to determine field values at the interfaces of Lagrangian Voronoi cells [28] or at molecular particles which exist only in an overlap band near the interfaces between Voronoi cells of the larger mesoscale particles [29]. The latter method in particular has some similarity with FVPM in its exploitation of a particle overlap region, although the motivation is quite different.

As in conventional finite volume discretisations [30–32], the linear reconstruction $\phi(\mathbf{x})$ should be defined so that the discrete particle value ϕ_i is recovered exactly in Eq. (11). Inserting the barycentre-centred linear reconstruction $\phi(\mathbf{x}) = \phi_i + \nabla\phi_i \cdot (\mathbf{x} - \mathbf{b}_i)$ into Eq. (11) for the discrete particle value,

$$\frac{1}{V_i} \int_{\Omega} [\phi_i + \nabla\phi_i \cdot (\mathbf{x} - \mathbf{b}_i)] \psi(\mathbf{x}) d\mathbf{x} \tag{31}$$

$$= \frac{1}{V_i} \int_{\Omega} \phi_i \psi(\mathbf{x}) d\mathbf{x} + \frac{\nabla\phi_i}{V_i} \left[\int_{\Omega} \mathbf{x} \phi(\mathbf{x}) d\mathbf{x} - \mathbf{b}_i \int_{\Omega} \phi(\mathbf{x}) d\mathbf{x} \right] \tag{32}$$

$$= \phi_i + \frac{\nabla\phi_i}{V_i} [V_i \mathbf{b}_i - V_i \mathbf{b}_i] \tag{33}$$

$$= \phi_i. \tag{34}$$

This shows that the sufficient condition to obtain the correct discrete value from the linear reconstruction is that the reconstruction be centred at the barycentre.

In the case of linear reconstruction, Barth [30] and Barth and Jespersen [33] have specified that the method used to determine the gradients should determine the gradient of a linearly varying field exactly. Finite volume methods commonly use a linear least squares reconstruction to satisfy this requirement on unstructured meshes [30]. The current approach uses the consistency corrected SPH gradient approximation of Bonet and Lok [11], which ensures that the gradient of a linearly varying field variable ϕ is reproduced exactly, even if the particles are disordered:

$$\nabla \phi_i \approx \sum_{j=1}^N V_j (\phi_j - \phi_i) \tilde{\nabla} S_j(\mathbf{b}_i), \tag{35}$$

where $S_i(\mathbf{x}) = S(\mathbf{x} - \mathbf{b}_i, q)$ denotes the SPH kernel function, with smoothing length q . S is distinct from the FVPM kernel function W . $\tilde{\nabla} S_j(\mathbf{b}_i)$ is the corrected gradient of the SPH kernel centred at \mathbf{b}_j and evaluated at \mathbf{b}_i :

$$\tilde{\nabla} S_j(\mathbf{b}_i) = \left[\sum_{l=1}^N V_l \nabla S_l(\mathbf{b}_i) \otimes (\mathbf{b}_l - \mathbf{b}_i) \right]^{-1} \nabla S_j(\mathbf{b}_i). \tag{36}$$

In two dimensions, Eq. (36) requires inversion of a 2×2 matrix for each particle. This matrix may become singular in the unlikely event that a particle and all its neighbours are collinear. In practical computations we have not found the invertibility of this matrix to be a problem.

The widely used cubic spline kernel of Monaghan and Lattanzio [34] is chosen for S :

$$S_i(\mathbf{x}) = \frac{\sigma}{q^D} \begin{cases} 1 - \frac{3}{2} \left| \frac{\mathbf{x} - \mathbf{b}_i}{q} \right|^2 + \frac{3}{4} \left| \frac{\mathbf{x} - \mathbf{b}_i}{q} \right|^3, & \text{if } 0 \leq \left| \frac{\mathbf{x} - \mathbf{b}_i}{q} \right| < 1.0, \\ \frac{1}{4} \left(2 - \left| \frac{\mathbf{x} - \mathbf{b}_i}{q} \right| \right)^3, & \text{if } 1.0 \leq \left| \frac{\mathbf{x} - \mathbf{b}_i}{q} \right| < 2.0, \\ 0, & \text{otherwise,} \end{cases} \tag{37}$$

where $\sigma = 2/3, 10/(7\pi), 1/\pi$ for space dimensions $D = 1, 2, 3$, respectively. The SPH kernel support radius $2q$ is chosen to be twice the FVPM particle radius $2h$. This is necessary to ensure an adequate number of neighbours for the SPH operation. FVPM particles interact with any overlapping particles, but SPH particles interact when they lie within each other's support. Therefore, the choice $q = 2h$ guarantees exactly the same number of neighbours and the same interaction radius for the SPH gradient evaluation as for the main FVPM operations. Using the computed gradients at the barycentre of particle i , the required field variable ϕ is reconstructed to the point $\mathbf{x}_{ij} = 1/2(\mathbf{x}_i + \mathbf{x}_j)$, which, when $h_i = h_j$, is the midpoint of the overlap region between the particles i and j :

$$\phi(\mathbf{x}_{ij})_i = \phi_i + \varphi_i \nabla \phi_i \cdot (\mathbf{x}_{ij} - \mathbf{b}_i), \tag{38}$$

where φ is a slope limiter function which ensures that the solution is monotone near discontinuities. In the present work this is used only for the shock tube test case (Section 6.1). The chosen slope limiter function is due to Barth and Jespersen [33], given by

$$\varphi_i(\mathbf{x}_{ij}) = \begin{cases} \min \left(1, \frac{\phi_i^{max} - \phi_i}{\nabla \phi_i \cdot (\mathbf{x}_{ij} - \mathbf{b}_i)} \right), & \text{if } \nabla \phi_i \cdot (\mathbf{x}_{ij} - \mathbf{b}_i) > 0, \\ \min \left(1, \frac{\phi_i^{min} - \phi_i}{\nabla \phi_i \cdot (\mathbf{x}_{ij} - \mathbf{b}_i)} \right), & \text{if } \nabla \phi_i \cdot (\mathbf{x}_{ij} - \mathbf{b}_i) < 0, \\ 1, & \text{if } \nabla \phi_i \cdot (\mathbf{x}_{ij} - \mathbf{b}_i) = 0, \end{cases} \tag{39}$$

where ϕ_i^{min} is the minimum value of ϕ evaluated at particle i and all its neighbours, and ϕ_i^{max} is similarly defined. The limiter for particle i is then chosen as $\varphi_i = \min[\varphi_i(\mathbf{x}_{ij})]$ for all particles j in the neighbourhood of i . Finally, the inviscid flux between particles i and j is computed using the limited, reconstructed quantities, i.e. $\mathcal{F}(\mathbf{U}_i(\mathbf{x}_{ij}), \mathbf{U}_j(\mathbf{x}_{ij}))$.

The formulation of the FVPM allows the use of numerical flux functions developed for conventional CFD methods. In this work, discretisation of the inviscid fluxes is performed using the AUSM⁺ scheme of Liou [35], which can easily be extended to equations of state other than Eq. (5). The particle motion terms are included using an ALE-type extension of the scheme, as presented by Luo et al. [36] and Smith [37]. In summary, the interface flux is computed from

$$\mathcal{F}(\mathbf{U}_i, \mathbf{U}_j) = a_{ij} M_{ij} \begin{pmatrix} \rho \\ \rho \mathbf{u} \\ \rho E + p \end{pmatrix}_{i/j} + \begin{pmatrix} 0 \\ p_{ij} \mathbf{n}_{ij} \\ p_{ij} \tilde{\mathbf{x}} \cdot \mathbf{n}_{ij} \end{pmatrix}, \tag{40}$$

where the interface sound speed is the average $a_{ij} = \frac{1}{2}(a_i + a_j)$, \mathbf{n}_{ij} is the unit vector $\beta_{ij}/|\beta_{ij}|$, the interface Mach number is defined as $M_{ij} = \mathcal{M}^+(M_i) + \mathcal{M}^-(M_j)$, and the interface pressure is written as $p_{ij} = \mathcal{P}^+(M_i)p_i + \mathcal{P}^-(M_j)p_j$. The relative particle Mach number is $M_i = ((\mathbf{u}_i - \tilde{\mathbf{x}}) \cdot \mathbf{n}_{ij})/a_{ij}$, and

$$(\bullet)_{ij} = \begin{cases} (\bullet)_j, & \text{if } M_{ij} < 0, \\ (\bullet)_i, & \text{otherwise.} \end{cases} \quad (41)$$

The Mach number and pressure splittings are defined by

$$\mathcal{M}^\pm(M) = \begin{cases} \frac{1}{2}(M \pm |M|), & \text{if } |M| > 1, \\ \pm \frac{1}{4}(M \pm 1)^2 \pm \kappa(M^2 - 1)^2, & \text{otherwise} \end{cases} \quad (42)$$

with $\kappa = 1/8$, and

$$\mathcal{P}^\pm(M) = \begin{cases} \frac{1}{2}(1 \pm \text{sign}(M)), & \text{if } |M| > 1 \\ \frac{1}{4}(M \pm 1)^2(2 \mp M) \pm \alpha M(M^2 - 1)^2, & \text{otherwise} \end{cases} \quad (43)$$

with $\alpha = 3/16$.

4.2. Viscous fluxes

Extension of the FVPM to viscous flows requires that the viscous fluxes be evaluated at each particle–particle interface. In particular, velocity gradients are required to compute the viscous stresses. These gradients are computed at the interface point \mathbf{x}_{ij} between each pair of particles using the corrected SPH gradient approximation Eq. (35), centred at \mathbf{x}_{ij} . The numerical approximation to the viscous flux \mathcal{G} is then computed using these gradients.

The viscous flux at the boundary \mathcal{G}^b is obtained using the corrected SPH gradient approximation for the velocity gradients:

$$\nabla \mathbf{u}^b \approx \sum_{j=1}^N V_j(\mathbf{u}_j - \mathbf{u}^b) \otimes \tilde{\nabla} S_j(\mathbf{x}^b) \quad (44)$$

with the corrected kernel gradient

$$\tilde{\nabla} S_j(\mathbf{x}^b) = \left[\sum_{j=1}^N V_j \nabla S_j(\mathbf{x}^b) \otimes (\mathbf{b}_j - \mathbf{x}^b) \right]^{-1} \nabla S_j(\mathbf{x}^b), \quad (45)$$

where \mathbf{x}^b is the midpoint of the boundary segment covered by the particle. \mathbf{u}^b is set to the appropriate boundary value. For example, in the implementation of a stationary no-slip wall, the velocity gradient would be computed using Eq. (44) with $\mathbf{u}^b = \mathbf{0}$.

4.3. Temporal discretisation

When the higher-order inviscid flux discretisation is employed, an explicit two-stage predictor–corrector scheme is used for the discretisation of the transient terms in Eq. (22). The algorithm follows that described by Hirsch [32] for a scheme based on linear reconstruction:

$$(V_i \mathbf{U}_i)^* = (V_i \mathbf{U}_i)^n - \frac{\Delta t}{2} \sum_{j=1}^N \beta_{ij} [\mathcal{F}(\mathbf{U}_i, \mathbf{U}_j) - \mathcal{G}_{ij}] - \beta_i^b [\mathcal{F}_i^b - \mathcal{G}_i^b], \quad (46)$$

$$(V_i \mathbf{U}_i)^{n+1} = (V_i \mathbf{U}_i)^n - \Delta t \sum_{j=1}^N \beta_{ij} [\mathcal{F}(\mathbf{U}_i^*(\mathbf{x}_{ij}), \mathbf{U}_j^*(\mathbf{x}_{ij})) - \mathcal{G}_{ij}^*] - \beta_i^b [\mathcal{F}_i^b(\mathbf{U}_i^*(\mathbf{x}^b)) - \mathcal{G}_i^b]. \quad (47)$$

The timestep Δt is restricted by the CFL stability condition [32]

$$\Delta t \leq C \frac{h_{\min}}{\lambda_{\max}}, \quad (48)$$

where C is the Courant number, and is set to 0.3 throughout this work. $\lambda_{\max} = \max(|\mathbf{u}| + a)$ is the maximum sound wave speed. The viscous diffusion condition must also be satisfied for viscous flows [6]

$$\Delta t \leq 0.25 \frac{\rho_{\min} h_{\min}^2}{\mu}. \quad (49)$$

Eq. (49) becomes the dominant timestep restriction at low Reynolds numbers.

5. Particle motion correction

In some of the numerical examples presented in Section 6, fully Lagrangian particle motion has been problematic due to the development of poor particle distributions, which in some cases can lead to simulation failure. This is characteristic of Lagrangian methods, since the particle distribution can be fully prescribed only for the initial condition, and is subsequently

determined by the flow. Chaniotis et al. [38] addressed this problem in SPH with a “remeshing” procedure in which the particles are reinitialised at regular intervals by interpolation onto a regular grid. For moving particle computations in FVPM, Schick [18] introduced non-Lagrangian particle motion in an effort to maintain adequate particle spacing for a 1-D problem with a discontinuous velocity field. In this work we propose and demonstrate a formulation for multidimensional non-Lagrangian motion, henceforth referred to as particle motion correction.

In particle motion correction, the particle motion velocity $\dot{\mathbf{x}}_i$ is equal to the fluid velocity \mathbf{u}_i plus a correction velocity \mathbf{u}'_i :

$$\dot{\mathbf{x}}_i = \mathbf{u}_i + \mathbf{u}'_i. \quad (50)$$

The correction velocity is given by

$$\mathbf{u}'_i = C \frac{\bar{r}_i}{\Delta t} \mathbf{R}_i, \quad (51)$$

where

$$\bar{r}_i = \frac{1}{H_i} \sum_k r_{ik} \quad (52)$$

is the average particle spacing in the neighbourhood of i , where the index k denotes the neighbours of i . Δt is the timestep, and C is a constant which is set to $1/1000$ for the computations presented in this article. H_i denotes the number of neighbours of particle i . The term $\bar{r}_i/\Delta t$ represents the velocity required for a particle to move by the average particle spacing \bar{r}_i in a single timestep Δt . \mathbf{R}_i is a dimensionless function of the inverse of the sum of particle spacings:

$$\mathbf{R}_i = \sum_k \frac{1}{\left(\frac{r_{ik}}{\bar{r}_i}\right)^2} \mathbf{n}_{ik}, \quad (53)$$

where r_{ik} and \mathbf{n}_{ik} are the distance and unit vector, respectively, from particle i to particle k .

In FVPM, no particles are located on the boundary or outside the domain. This leads to a particle deficiency in Eq. (53) for particles near boundaries, which we remedy by including an additional point in the summation. This point is selected as the midpoint of the boundary segment that lies inside the particle support.

The crucial feature of this particle motion correction is that it acts as a weak repulsion between particles which suppresses particle clumps and voids. This is not a spurious non-physical force in the field, but rather a simple means of dynamically controlling particle distribution. In contrast with fully Lagrangian FVPM or SPH, the motion of the computational particles is slightly decoupled from the physical fluid motion. The corrected particle motion is accounted for through the $\dot{\mathbf{x}}$ term in Eq. (19), which makes the scheme an Arbitrary Lagrange–Euler (ALE) method. No interpolation procedure is required to deal with the modified particle positions. The particle motion remains close to Lagrangian because of the small value of C . In the examples shown in this paper, we have found that the particle motion correction velocity, \mathbf{u}' , is typically less than 5% of the maximum velocity in the field.

6. Results

The extensions to the FVPM presented in Sections 4 and 5 are validated in this section. Firstly, the higher-order spatial and temporal discretisations presented in Sections 4.1 and 4.3 are validated for inviscid flow by means of a 1-D shock tube test case. The FVPM for viscous flow is validated for Poiseuille flow using both the first and higher-order versions of the scheme. Finally, validations for Taylor–Green flow and flow in a lid-driven cavity are presented as examples of more complex viscous flows.

6.1. Shock tube

The 1-D shock tube is selected as a test case for the inviscid higher-order extension of the FVPM presented in this paper. This well-known test case is commonly used to assess the performance of compressible flow algorithms. The problem consists of a 1-D tube in the region $-L \leq x \leq L$ with initial pressure $p = p_l$ for $x \leq 0$ and $p = p_r$ for $x > 0$, where $p_r/p_l = 0.25$ in this case. The initial velocity is zero everywhere. Four hundred particles are initially uniformly distributed along the tube, which is of total length $2L$, and the smoothing length of all particles is set to $h = 0.8\Delta x$, where Δx is the initial particle spacing. The volume of each particle is initialised using numerical integration of Eq. (10). The particles are fully Lagrangian – that is, $\dot{\mathbf{x}} = \mathbf{u}$ and no particle motion correction is applied. Results are presented for both the first-order FVPM and the higher-order extension of the method, as described in Sections 4.1 and 4.3. For the higher-order version of the scheme, the slope limiter function of Eq. (39) is used to prevent oscillations occurring near discontinuities in the solution.

Fig. 1 shows the pressure distribution for the first and higher-order methods at time $t^* = ta_0/L = 0.3$, where a_0 is the initial speed of sound in the tube. The first-order solution requires approximately 12 particles to resolve the shock. The higher-order extension of the method, on the other hand, shows a greatly enhanced shock-capturing ability, capturing the shock within approximately five particles, and also predicts the expansion wave more accurately than the first-order scheme.

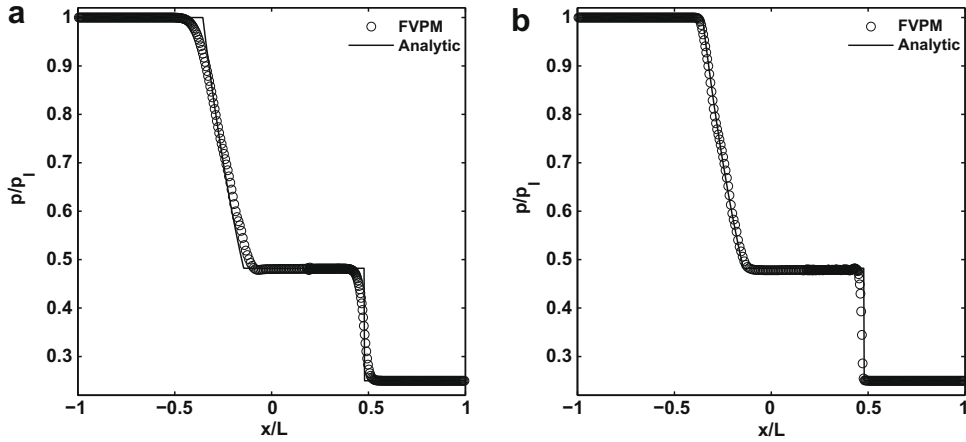


Fig. 1. Instantaneous pressure distribution in shock tube at dimensionless time $t^* = 0.3$. (a): First-order FVPM and (b): higher-order FVPM.

This test case has also been solved using Eulerian particles, i.e. $\dot{\mathbf{x}} = 0$. This yielded a slight improvement in the results near the contact surface, due to the more regular particle distribution. In the Lagrangian case, the density discontinuity results in a highly non-uniform particle distribution in this region.

6.2. Poiseuille flow

The viscous implementation of the FVPM is validated for plane Poiseuille flow. This test case consists of incompressible viscous flow between two infinite stationary parallel plates. The flow accelerates from rest under an axial applied body force. The channel is modelled in the $x - y$ plane, with the x -axis representing the flow direction and with the plates located at $y = \pm d$. The axial velocity $u(y, t)$ in the channel is obtained from the series solution [6,7]

$$u(y, t) = \frac{g\rho}{2\mu} (d^2 - y^2) - \sum_{n=0}^{\infty} \left\{ \frac{(-1)^n 16d^2 g\rho}{\mu\pi^3 (2n+1)^3} \cos \left[\frac{(2n+1)\pi y}{2d} \right] \exp \left[-\frac{(2n+1)^2 \pi^2 \mu t}{4d^2 \rho} \right] \right\}, \quad (54)$$

where g is a uniform and constant force per unit mass. As $t \rightarrow \infty$, Eq. (54) approaches the steady-state solution

$$u(y) = u_0 \left(1 - \frac{y^2}{d^2} \right) = \frac{g\rho}{2\mu} (d^2 - y^2), \quad (55)$$

where u_0 is the steady-state centreline velocity.

The plane Poiseuille flow has been simulated for Reynolds numbers (based on u_0 and $2d$) of $Re = 0.0125$ and $Re = 200$ using both the first-order and higher-order versions of FVPM. Incompressible flow is modelled using the weakly compressible equation of state Eq. (7). The peak Mach number in all cases is specified as $M = 0.1$ by setting the numerical speed of sound a_0 appropriately. The choice of $Re = 0.0125$ coincides with the value used for Poiseuille flow computations presented in the SPH literature [6,7]. The particles are initially arranged in a regular Cartesian pattern. No fictitious wall particles are required to compute the Poiseuille flow problem using FVPM. The initial particle volumes are computed using numerical integration of Eq. (10) and the smoothing length of all particles is $h = 0.7\Delta x$, where Δx is the initial particle spacing.

The transient evolution of the u velocity profile across the channel for both the FVPM and the series solution is shown in Fig. 2 for $Re = 0.0125$. In this case, 25 particles are distributed across the channel width, and the particle motion is Lagrangian. At $t^* = tu_0/(2d) = 0.0125$, the solution is close to steady-state. At such a low Reynolds number, the discretisation of the inviscid fluxes has little or no effect on the velocity profiles, and good agreement between the FVPM and series solution is achieved using both the first and higher-order versions of the scheme.

To assess the error properties of the scheme for Poiseuille flow at $Re = 0.0125$, the flow was computed with 10, 25, 50 and 100 particles across the channel width, with the higher-order extensions described in Section 4.1. A dimensionless L_∞ error norm was computed as follows:

$$L_\infty(t^*) = \max \left| \frac{u_i^{th}(t^*) - u_i^{num}(t^*)}{u_0} \right|, \quad (56)$$

where $u^{th}(t)$ and $u^{num}(t)$ are the analytic and FVPM velocities, respectively. Fig. 3(a) shows the instantaneous L_∞ error as a function of the particle spacing Δx for time $t^* = 1 \times 10^{-3}$. The order of convergence is slightly less than 2 for both the Eulerian and Lagrangian cases.

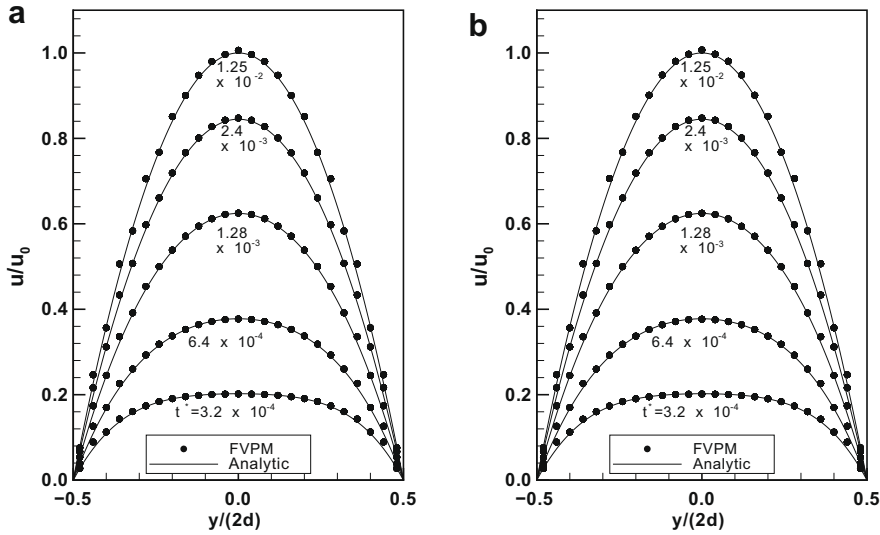


Fig. 2. Non-dimensionalised transient Poiseuille flow velocity profiles at various times $t^* = tu_0/(2d)$ for $Re = 0.0125$ with Lagrangian particle motion. (a) First-order and (b) higher-order version of the scheme.

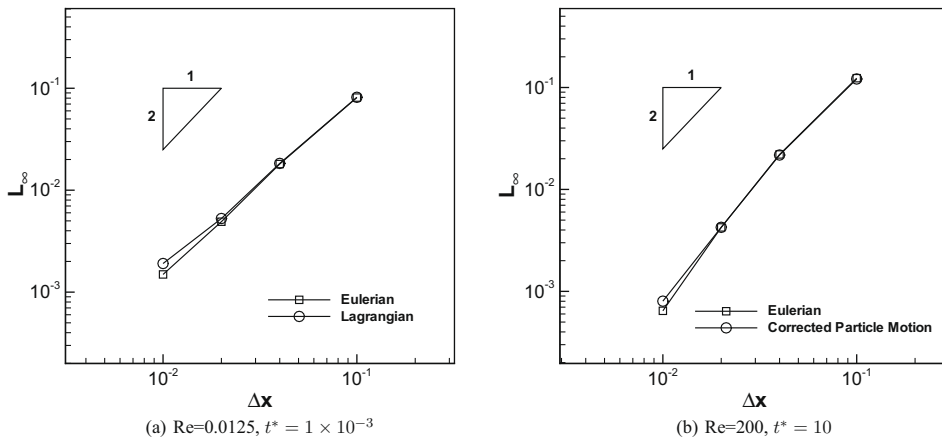


Fig. 3. Poiseuille flow with higher-order FVPM: instantaneous variation of L_∞ error with Δx for Eulerian, Lagrangian or corrected particle motion.

Poiseuille flow has also been simulated at the higher Reynolds number of $Re = 200$ using FVPM. At this Reynolds number, the dimensionless time t^* required to reach a steady-state is much greater than for the $Re = 0.0125$ case, and consequently the particle displacement from the initial distribution is much greater at the onset of steady-state. For Lagrangian particle motion at $t^* = 46$, the particle distribution is shown in Fig. 5(a). In principle, such a particle distribution should not develop for Poiseuille flow, since the transverse velocity, and hence transverse particle motion, should be identically zero. However, numerical errors result in transverse drift of particles. A slight deviation from streamwise alignment of the particles is sufficient to result in a poor particle distribution, and ultimately simulation failure. This phenomenon has also been observed in SPH computations for Poiseuille flow by Basa et al. [39]. The corrected particle motion described in Section 5 improves this situation, and the resulting particle distribution at $t^* = 46$ is shown in Fig. 5(b).

In addition to the particle distribution problem experienced for Poiseuille flow at $Re = 200$, we have experienced problems with inaccurate evolution of the particle volumes for moving particles. This problem is characterised by variations in the particle volume even in regions where the particle spacing is uniform. This behaviour influences the density and pressure fields, and can result in simulation failure. As a remedy for this problem, we periodically re-compute the volume of each particle using Eq. (10) rather than the volume evolution equation Eq. (25). For the results presented here, the volumes are re-computed every 20 timesteps.

The transient evolution of the streamwise velocity profile is shown in Fig. 4 for corrected particle motion and the higher Reynolds number of $Re = 200$, with 25 particles distributed across the channel width. For this computation, the solution is

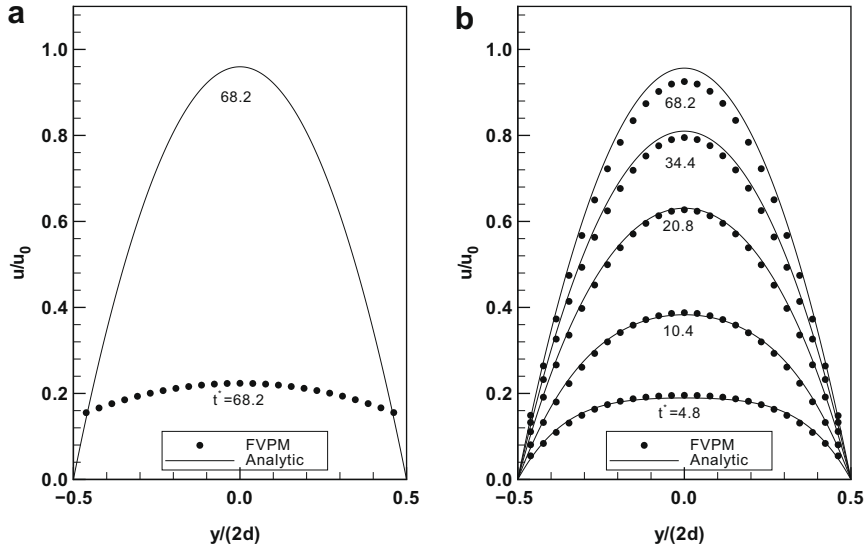


Fig. 4. Non-dimensionalised transient Poiseuille flow velocity profiles at various times $t^* = tu_0/(2d)$ for $Re = 200$ with corrected particle motion. (a) First-order and (b) higher-order version of the scheme.

close to steady-state at $t^* = 68.2$. In this case, the inviscid flux discretisation has a significant impact on the accuracy of the results. The first-order version of the method is extremely diffusive and fails to produce accurate velocity profiles. On the other hand, the higher-order version of the method produces velocity profiles that are in good agreement with the series solution at all times.

The variation of L_∞ error with initial particle spacing is shown in Fig. 3(b) for time $t^* = 10$. In this case, slightly higher convergence rates are observed than in the case of $Re = 0.0125$, and the effect of the particle motion on accuracy is minimal.

6.3. Taylor–Green flow

Taylor–Green flow is used to assess the error behaviour of the method for a more complex incompressible, viscous, two-dimensional flow. This flow field consists of a periodic array of decaying vortices, and is defined by the following analytical solution:

$$u(x, y, t) = -u_0 \cos\left(\frac{2\pi x}{L}\right) \sin\left(\frac{2\pi y}{L}\right) e^{-\frac{8\pi^2 \nu t}{L^2}}, \tag{57}$$

$$v(x, y, t) = u_0 \sin\left(\frac{2\pi x}{L}\right) \cos\left(\frac{2\pi y}{L}\right) e^{-\frac{8\pi^2 \nu t}{L^2}}, \tag{58}$$

$$p(x, y, t) = -\frac{1}{4} \left[\cos\left(\frac{4\pi x}{L}\right) + \cos\left(\frac{4\pi y}{L}\right) \right] e^{-\frac{16\pi^2 \nu t}{L^2}}, \tag{59}$$

where u_0 is the peak initial velocity and L is the length of the domain side.

This flow was modelled at Reynolds number 100 (based on u_0 and L) for particle resolutions of 20×20 , 40×40 , 60×60 and 100×100 using the higher-order FVPM scheme only. The smoothing lengths were initialised to $h = 0.8\Delta x_0$, where Δx_0 denotes the initial uniform Cartesian particle spacing, and remained constant for the duration of the computation. A single vortex cell was modelled in a domain with periodic boundaries at $x = \pm L/2$ and $y = \pm L/2$. The velocity and pressure were initialised according to Eqs. (57)–(59) evaluated at $t = 0$. Incompressible flow was modelled using the weakly compressible equation of state Eq. (7). The reference sound speed a_0 was set to $10u_0$, and for the purposes of this test case, the timestep Δt was set to $\Delta x_0/a_0$. The computation was allowed to proceed until the maximum velocity in the domain decayed below $u_0/10$. Simulations were carried out with Eulerian (stationary) particles, fully Lagrangian particle motion and corrected particle motion. In all these cases the particles were initialised in a uniform Cartesian distribution. In a fourth test, particles were initialised in a uniform Cartesian arrangement and then randomly shifted by a displacement between $-h/2$ and $+h/2$ (with uniform probability) in both the x and y directions, before initiating the simulation with fully Lagrangian motion. This additional case was included to investigate the effect of the initial particle distribution, which is known to be significant for SPH methods [40].

For $Re = 100$, with 3600 particles in corrected particle motion, the maximum velocity history is shown in Fig. 6, showing good agreement between the FVPM and analytic solutions. Fig. 7 shows the particle positions and velocity vectors at dimensionless time $t^* = tu_0/L = 0.2$ with Lagrangian and corrected particle motion. For Lagrangian particle motion from an initial

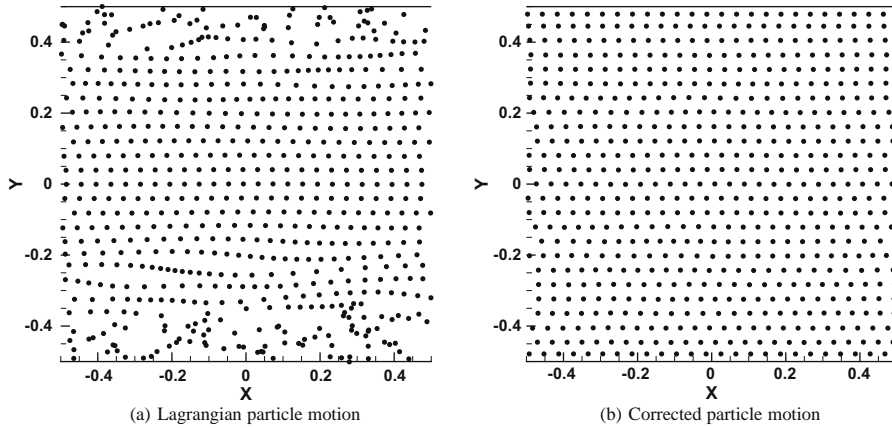
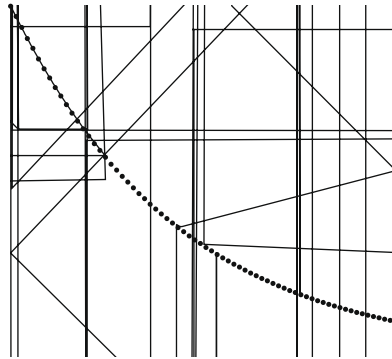


Fig. 5. Particle positions for Poiseuille flow at $Re = 200$ and $t^* = 46$.



distribution, the particle distribution is highly non-uniform and anisotropic. The situation is improved somewhat with the corrected initial distribution. With corrected particle motion (Fig. 7c), a uniform particle spacing is maintained for the duration of the computation.

Figure 6 shows the non-dimensional L_∞ error norm

$$\frac{\max_i |u_i^{th}(t^*) - u_i^{num}(t^*)|}{u_0} \quad (60)$$

Figure 7 shows the results for the various particle motion formulations and initialisations. For Lagrangian particle motion with the corrected initial condition, the computation fails in the early stages. For Lagrangian particle motion with the corrected initial condition and corrected particle motion, the simulation does not fail, though the L_∞ error norm is characterised by large transient spikes. The error norm is significantly improved by the use of corrected particle motion, for which the magnitude of the error norm is significantly reduced.

Figure 8 shows the convergence of the error norm on particle spacing Δx at time $t^* = 1.5$ is shown in Fig. 9 for both Eulerian particles and Lagrangian particles. The convergence is close to second order, and the effect of particle motion on the convergence is minimal.

(61)

Figure 9 compares the convergence of the error norm for SPH results from the literature [40]. For Eulerian particles and corrected particle motion, the convergence is significantly lower than the results of both SPH variants. For Lagrangian particles, the convergence is similar to the Eulerian case, but is larger than the error in weakly compressible SPH.

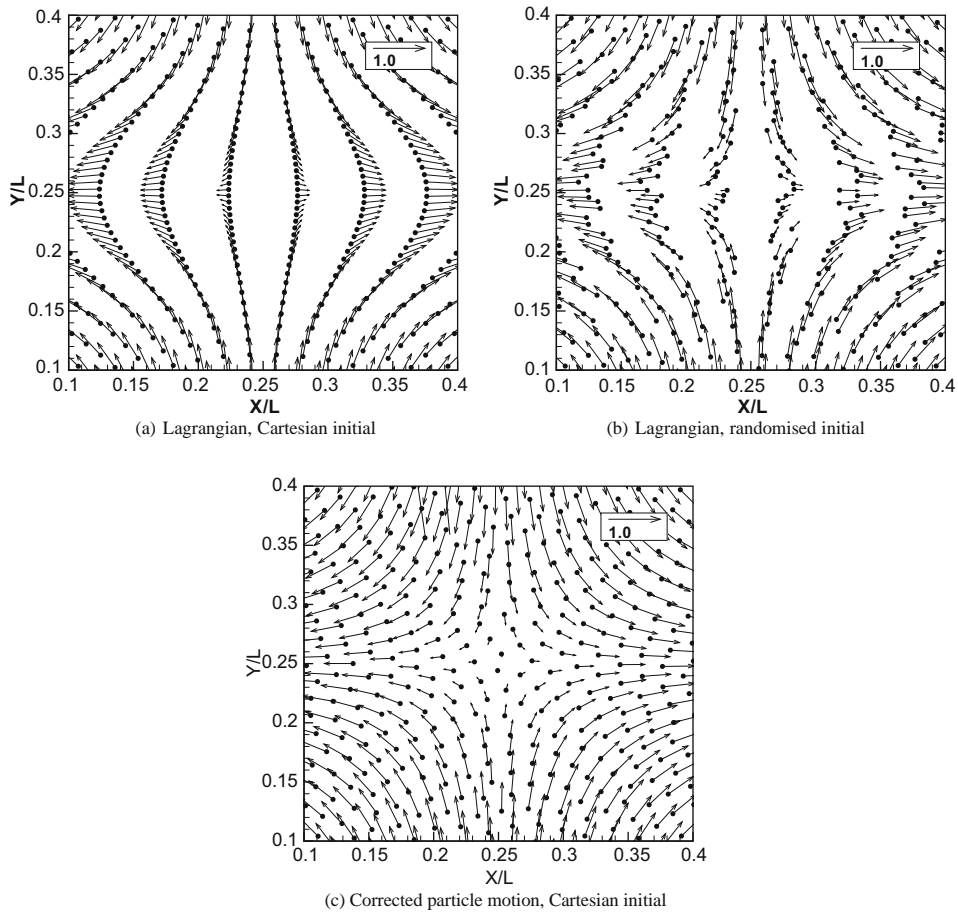


Fig. 7. Particle positions and velocity vectors near one of the stagnation points for Taylor–Green flow at $t^* = 0.2$. (a): Lagrangian particle motion, uniform Cartesian initial distribution. (b): Lagrangian particle motion, randomised initial distribution. (c): Corrected particle motion, Cartesian initial distribution.

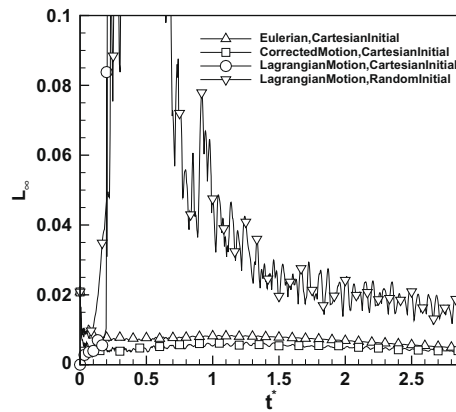


Fig. 8. Transient behaviour of L_∞ error for Taylor–Green flow at $Re = 100$ with 3600 FVPM particles, for various treatments of particle motion and initial particle distribution.

6.4. Lid-driven cavity

Another well-known test case for viscous incompressible flow is the lid-driven cavity. This test consists of a square domain with no-slip walls of length L on all sides. The wall at $y^* = y/L = 0.5$ moves with a constant tangential velocity u_l , causing the fluid to circulate within the cavity, eventually approaching a steady-state. A FVM reference solution generated using

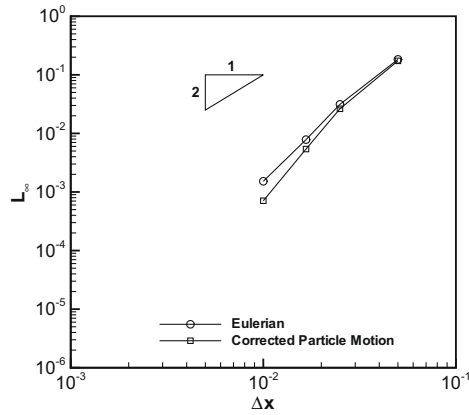


Fig. 9. Variation of instantaneous L_∞ error with particle spacing at $t^* = 1.5$ for Taylor–Green flow at $Re = 100$.

Table 1

$L_2 (\times 10^2)$ error norms for Taylor–Green flow at $Re = 100$ with 3600 particles for FVPM with Eulerian particles, corrected particle motion and Lagrangian particle motion with random initial distribution. Also shown are incompressible SPH (ISPH) and weakly compressible SPH (WCSPH) results from the literature [40].

t^*	$L_2 (\times 10^2)$				
	Eulerian	Corrected motion	Lagrangian	ISPH [40]	WCSPH [40]
0.9	0.379	0.271	1.097	4.707	1.747
1.8	0.353	0.262	1.009	2.640	0.807
2.7	0.250	0.185	0.684	1.432	0.309

the OpenFOAM 1.4.1 CFD package [41] with the PISO algorithm on a 300×300 mesh, and the high-resolution numerical results of Ghia et al. [42], are used for the purposes of validation. Weakly compressible SPH results are also used for comparison. This SPH simulation was carried out with 50×50 particles, first-order consistency correction [11], and the viscosity model of Cleary [43].

The Reynolds number (based on u_l and L) is 1000. The particles are initially arranged in a regular Cartesian pattern, and the smoothing length is set to $h = 0.7\Delta x_0$, where Δx_0 is the initial particle spacing. All particles have zero initial velocity and uniform initial density and pressure. The initial particle volume is computed using numerical integration of Eq. (10). Incompressible flow is modelled using the weakly compressible equation of state, Eq. (7). The reference speed of sound a_0 is chosen so that the maximum Mach number is less than 0.1 at all times. Results are presented for both Eulerian particles and corrected particle motion. Fully Lagrangian simulations failed due to the development of poor particle distributions, regardless of the initial particle distribution. The instantaneous particle positions prior to simulation failure for fully Lagrangian particle motion is shown in Fig. 10(a). The corresponding particle positions for corrected particle motion is shown in Fig. 10(b). For moving particles, the volumes are periodically re-computed as described in Section 6.2.

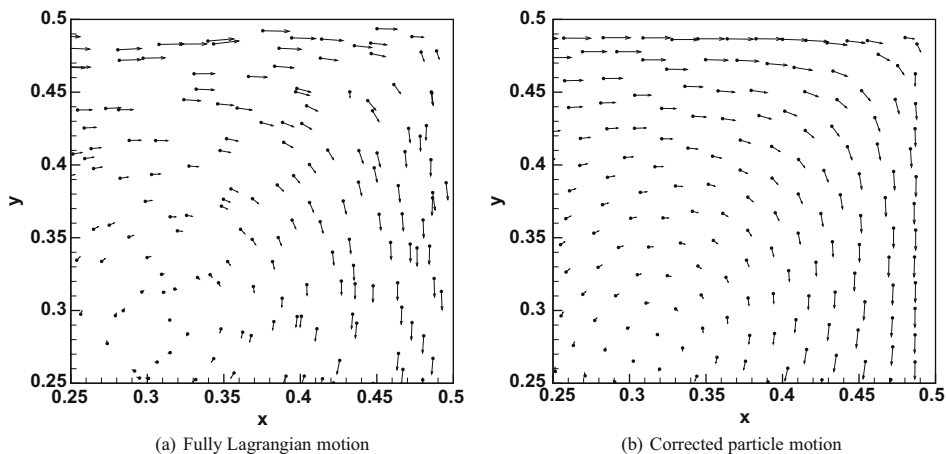


Fig. 10. Particle positions and velocity vectors in the upper right corner of the lid-driven cavity at $t^* = 3.3$ and $Re = 1000$ with Lagrangian and corrected particle motion Eq. (50).

The steady-state solution is characterised by a downward flow in the upper right corner of the cavity, and a recirculating region in the centre of the domain. The steady-state x -velocities at the domain centreline $x = 0$ are used for the purposes of comparing the FVPM results with the reference solution. Fig. 11 shows a comparison between the velocity profile of [42]Ghia et al. [42], the FVM reference solution, and the FVPM velocity profiles for particle numbers of 50×50 , 75×75 and 100×100 . The centreline velocity profile is accurately predicted, and the FVPM velocity profiles converge towards the reference solutions as the number of particles is increased. FVPM with 50×50 particles is significantly more accurate than the comparable SPH simulation.

As a further comparison, the non-dimensional total kinetic energy as a function of time is shown in Fig. 12. FVPM results are provided for 50×50 particles with both Eulerian and corrected particle motion. All of the mesh-free solutions underestimate the total kinetic energy relative to the finite volume solution. However, the FVPM results are in closer agreement with the finite volume reference solution than the SPH results at similar resolution. There is a small difference in kinetic energy values between the Eulerian and moving particle FVPM cases.

6.5. Computational cost

For FVPM with moving particles, the most computationally expensive part of the method is the generation of the geometric coefficients. In the present algorithm, computation of the coefficients takes 86% of the total computational time. The bary-centre computation, the finite volume element of the algorithm, and the SPH-based linear reconstruction require 5%, 4% and 0.9% of the total computational time respectively. Neighbour searching comprises 1.5% of the total computational effort. Computation of the particle volumes via Eq. (10) requires a negligible fraction of the total time. These proportions remain approximately constant with varying particle numbers.

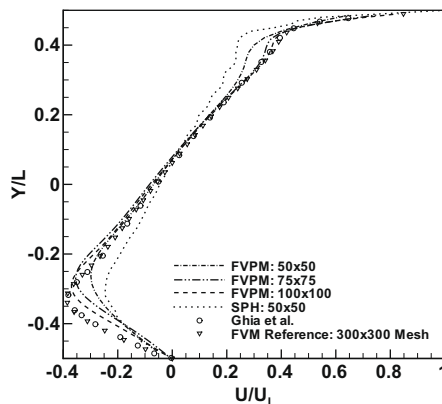


Fig. 11. x component of velocity along the lid-driven cavity centreline $x = 0$ for $Re = 1000$: FVPM with 50×50 , 75×75 and 100×100 particles, SPH with 50×50 particles, finite volume reference solution with 300×300 mesh, and high-resolution result of Ghia et al. [42], FVPM particles move with corrected particle motion.

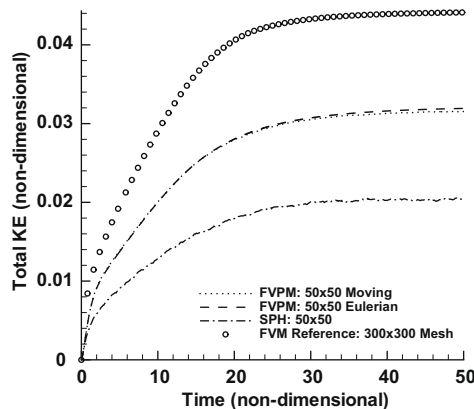


Fig. 12. Total kinetic energy for lid-driven cavity flow at $Re = 1000$: finite volume reference solution with 300×300 mesh, FVPM with 50×50 particles (Eulerian particles and corrected particle motion), and SPH with 50×50 particles.

7. Conclusions

A FVPM formulation for viscous flow has been presented and validated for two-dimensional flows at Reynolds numbers up to 1000. The application to viscous flows has been facilitated by several developments of the original FVPM. A higher-order formulation was developed, with an AUSM⁺ discretisation for inviscid fluxes. This was validated for inviscid shock tube flow, in which it showed greater accuracy than the first-order version. The higher-order extension was found to be a prerequisite for accurate viscous flow solutions at the higher Reynolds numbers. Secondly, viscous stress was computed in the FVPM using a consistency-corrected SPH approximation for the velocity gradients. Finally, a particle motion correction was implemented to prevent the development of poor particle distributions in Lagrangian mode. Although the departure from purely Lagrangian velocity is small, FVPM in this mode was shown to maintain relatively uniform particle distribution and to be almost as accurate as the fully Eulerian version. The developed FVPM method has exhibited near second-order convergence, and better accuracy than recent SPH results.

FVPM has a number of particularly attractive features as a mesh-free method, due largely to its roots in the finite volume method. It requires no fictitious boundary particles, ensures exact local conservation regardless of particle distribution, and can readily incorporate classical finite volume techniques such as upwind inviscid flux discretisations. The present work extends the scope of FVPM to laminar viscous flows at low and moderate Reynolds numbers. However, the method carries a significant additional cost due to the computation of the geometric coefficients β_{ij} , which requires further investigation. In other further work, the applicability of the method will be investigated in different classes of flows for which mesh-free methods are particularly suitable, such as free surface, multiphase and fluid–structure interaction problems.

Acknowledgment

This research is supported by Grant No. RS/2005/95 from the Irish Council for Science, Engineering and Technology, funded by the National Development Plan.

References

- [1] R. Gingold, J. Monaghan, Smoothed particle hydrodynamics: theory and application to non-spherical stars, *Monthly Notices of the Royal Astronomical Society* 181 (1977) 375–389.
- [2] L. Lucy, A numerical approach to testing the fission hypothesis, *The Astronomical Journal* 82 (1977) 1013–1024.
- [3] J. Monaghan, Simulating free surface flows with SPH, *Journal of Computational Physics* 110 (1994) 399–406.
- [4] S. Cummins, M. Rudman, An SPH projection method, *Journal of Computational Physics* 152 (1999) 584–607.
- [5] H. Takeda, S. Miyama, M. Sekiya, Numerical simulation of viscous flow by smoothed particle hydrodynamics, *Progress of Theoretical Physics* 92 (1994) 939–960.
- [6] J. Morris, P. Fox, Y. Zhu, Modelling low Reynolds number incompressible flows using SPH, *Journal of Computational Physics* 136 (1997) 214–226.
- [7] L. Sigalotti, J. Klapp, E. Sira, Y. Melean, A. Hasmy, SPH simulations of time-dependent Poiseuille flow at low Reynolds numbers, *Journal of Computational Physics* 191 (2003) 622–638.
- [8] J.J. Monaghan, Smoothed particle hydrodynamics, *Reports on Progress in Physics* 68 (2005) 1703–1759.
- [9] W. Liu, S. Jun, Y. Zhang, Reproducing kernel particle methods, *International Journal for Numerical Methods in Fluids* 20 (1995) 1081–1106.
- [10] P. Randles, L. Libersky, Smoothed particle hydrodynamics: some recent improvements and applications, *Computer Methods in Applied Mechanics and Engineering* 139 (1996) 375–408.
- [11] J. Bonet, T.-S.L. Lok, Variational and momentum preservation aspects of smooth particle hydrodynamic formulations, *Computer Methods in Applied Mechanics and Engineering* 180 (1999) 97–115.
- [12] J. Monaghan, SPH and Riemann Solvers, *Journal of Computational Physics* 136 (1997) 298–307.
- [13] J.P. Vila, P. Degond, On particle weighted methods and smooth particle hydrodynamics, *Mathematical Models and Methods in Applied Sciences* 9 (1999) 161–209.
- [14] G. Dilts, Moving least-squares particle hydrodynamics I: consistency and stability, *International Journal for Numerical Methods in Engineering* 44 (1999) 1115–1155.
- [15] G. Dilts, Moving least-squares particle hydrodynamics II: conservation and boundaries, *International Journal for Numerical Methods in Engineering* 48 (2000) 1503–1524.
- [16] T. Ismagilov, Smooth volume integral conservation law and method for problems in Lagrangian coordinates, *Computational Mathematics and Mathematical Physics* 46 (2006) 453–464.
- [17] D. Hietel, K. Steiner, J. Struckmeier, A finite volume particle method for compressible flows, *Mathematical Models and Methods in Applied Science* 10 (2000) 1363–1382.
- [18] C. Schick, Anisotropic smoothing kernels for particle methods in fluid flow, Master's thesis, University of Kaiserslautern, 2000.
- [19] B. Lamichhane, The applications of the finite volume particle method for moving boundary, Master's thesis, University of Kaiserslautern, 2000.
- [20] R. Keck, The finite volume particle method: a meshless projection method for incompressible flow, Ph.D. thesis, University of Kaiserslautern, 2002.
- [21] R. Keck, D. Hietel, A projection technique for incompressible flow in the meshless finite volume particle method, *Advances in Computational Mathematics* 23 (2005) 143–169.
- [22] D. Teleaga, A finite volume particle method for conservation laws, Ph.D. thesis, University of Kaiserslautern, 2005.
- [23] J. Kirkwood, H. Bethe, The pressure wave produced by an underwater explosion, OSRD Report, The Office of Scientific Research and Development, 1942.
- [24] D. Hietel, R. Keck, Consistency by coefficient correction in the finite volume particle method, in: M. Griebel (Ed.), *Meshfree Methods for Partial Differential Equations*, Lecture Notes in Computational Science and Engineering, Springer, 2003, pp. 211–221.
- [25] M. Junk, J. Struckmeier, Consistency analysis of meshfree methods for conservation laws, *Mitteilungen der Gesellschaft für Angewandte Mathematik und Mechanik* 24 (2001) 99–126.
- [26] D. Fulk, D. Quinn, An analysis of 1-D smoothed particle hydrodynamics kernels, *Journal of Computational Physics* 126 (1996) 165–180.
- [27] B. van Leer, Towards the ultimate conservative difference scheme. V – a second-order sequel to Godunov's method, *Journal of Computational Physics* 32 (1979) 101–136.
- [28] M. Serrano, P. Español, Thermodynamically consistent mesoscopic fluid particle model, *Physical Review E* 64 (2001) 046115–1–046115–18.
- [29] E.G. Flekkøy, P.V. Coveney, G. De Fabritiis, Foundations of dissipative particle dynamics, *Physical Review E* 62 (2000) 2140–2157.

- [30] T. Barth, Aspects of unstructured grids and finite volume solvers for the Euler and Navier–Stokes equations, in: 25th Computational Fluid Dynamics Lecture Series, Von Karman Institute for Fluid Dynamics, 1994.
- [31] R. LeVeque, Finite Volume Methods for Hyperbolic Problems, Cambridge University Press, Cambridge, 1995.
- [32] C. Hirsch, Numerical Computation of Internal and External Flows, Volume 2: Computational Methods for Inviscid and Viscous Flows, Wiley, Chichester, 1988.
- [33] T. Barth, D. Jespersen, The design and application of upwind schemes on unstructured meshes, in: AIAA 27th Aerospace Sciences Meeting, AIAA, 1989.
- [34] J. Monaghan, J. Lattanzio, A refined method for astrophysical problems, *Astronomy and Astrophysics* 149 (1985) 135–143.
- [35] M.-S. Liou, A sequel to AUSM: AUSM⁺, *Journal of Computational Physics* 129 (1996) 364–382.
- [36] H. Luo, J. Baum, R. Lohner, On the computation of multi-material flows using ALE formulation, *Journal of Computational Physics* 194 (2004) 304–328.
- [37] R. Smith, AUSM(ALE): a geometrically conservative arbitrary Lagrangian–Eulerian flux splitting scheme, *Journal of Computational Physics* 150 (1999) 268–286.
- [38] A.K. Chaniotis, D. Poulidakos, P. Koumoutsakos, Remeshed smoothed particle hydrodynamics for the simulation of viscous and heat conducting flows, *Journal of Computational Physics* 182 (2002) 67–90.
- [39] M. Basa, N.J. Quinlan, M. Lastiwka, Robustness and accuracy of SPH formulations for viscous flow, *International Journal of Numerical Methods in Fluids* (2008), in press, doi:10.1002/flid.1927.
- [40] M. Ellero, M. Serrano, P. Español, Incompressible smoothed particle hydrodynamics, *Journal of Computational Physics* 226 (2007) 1731–1752.
- [41] OpenCFD Ltd., OpenFOAM 1.4.1, <www.opencfd.co.uk> (accessed: 8 August 2008).
- [42] U. Ghia, K. Ghia, C. Shin, High-Re solutions for incompressible flow using the Navier–Stokes equations and a multigrid method, *Journal of Computational Physics* 48 (1982) 387–411.
- [43] P.W. Cleary, Modelling confined multi-material heat and mass flows using SPH, *Applied Mathematical Modelling* 22 (1998) 981–993.